Radiation Physics and Chemistry 190 (2022) 109759

Contents lists available at ScienceDirect

Radiation Physics and Chemistry

journal homepage: www.elsevier.com/locate/radphyschem

Production yields at the distal fall-off of the β^+ emitters ^{11}C and ^{13}N for in-vivo range verification in proton therapy

Teresa Rodríguez-González [a,b], Carlos Guerrero [a,b,*,1], María del Carmen Jiménez-Ramos [b], Jorge Lerendegui-Marco [a], María de los Ángeles Millán-Callado [a,b], Ángel Parrado [b], Joaquín Gómez [a,b], Jose Manuel Quesada [a]

[a] Dept. de Física Atómica, Molecular y Nuclear. Universidad de Sevilla, Avda. Reina Mercedes s/n, Seville, 41012, Spain
[b] Centro Nacional de Aceleradores (Universidad de Sevilla-Junta de Andalucía-CSIC), C/ Thomas Alva Edison 7, Seville, 41092, Spain

ARTICLE INFO

Keywords:
Nuclear cross section
β^+ emitters
Activation technique
PET scanner
Proton therapy
PET range verification

ABSTRACT

In proton therapy, Positron Emission Tomography (PET) range verification relies on the comparison of the measured and estimated activity distributions from β^+ emitters produced by the proton beam in the patient. The accuracy of the estimated activity distributions is basically that of the underlying reaction cross section data. In this context, we have developed a new method for measuring β^+ production yields combining the multi-foil technique with a clinical PET scanner, resulting in energy differential cross sections from a single irradiation. The method has been applied to the production of ^{11}C ($t_{1/2}$ = 20.36 min) and ^{13}N ($t_{1/2}$ = 9.97 min), the main candidates for off-line PET range verification, in carbon, nitrogen and oxygen, the main elements of the human body. The energy range studied with the 18 MeV CNA cyclotron corresponds to the distal fall-off of the activity curve, i.e. near the Bragg peak.

1. Introduction and motivation

In comparison to conventional radiation therapy, proton therapy is able to reduce the dose deposition in the healthy tissues close to the tumor thanks to the distinct characteristics of the spatial dose distributions of charged particles: maximum dose deposition near the end of their trajectory (the Bragg peak) and a finite penetration in matter. Proton therapy is hence especially well-suited for tumors close to organs at risk and in pediatric cases because of the lower dose received by healthy tissues, which reduces the long-term effects of the treatment, improving the quality of life of the patient (Knopf and Lomax, 2013). However, the current treatment plannings have to be quite conservative because there are uncertainties associated to the imaging, patient setup, beam delivery and dose calculations that can affect the actual range of the beam delivered. Indeed, a safety margin of up to 1 cm is considered nowadays for a prescribed range of 30 cm (Paganetti et al., 2012).

A way to reduce the mentioned safety margins and exploit proton therapy to its full potential is the verification of the beam range during or right after the irradiation. One possibility is to look at the activation map of the irradiated patient with a PET scanner, in particular at the two 511 keV photons emitted in opposite directions by β^+ unstable isotopes resulting from proton induced nuclear reactions (Kraan et al., 2015). The most abundant "long" half-life β^+ isotopes produced by protons in the human body are ^{11}C ($t_{1/2}$ = 20.36 min) and ^{13}N ($t_{1/2}$ = 9.97 min), both with a half-life long enough to allow moving the patient from the irradiation table to the PET scanner. However, the relationship between the dose and activity depth distributions is not straightforward (Oelfke et al., 1996; Parodi et al., 2007), so PET range verification can not rely only on the measurement of the activity depth profile, but on its comparison with the one estimated through Monte Carlo calculations combining information from the treatment planning with the cross sections for the nuclear reactions involved.

The main reaction channels for the production of ^{11}C and ^{13}N are shown in Fig. 1. At high energies, ^{11}C is mainly produced by ^{12}C, whereas ^{13}N is mainly produced by ^{14}N. However, below 20 MeV the dominant reaction channels are ^{14}N(p,α)^{11}C and ^{16}O(p,α)^{13}N. These are the typical reactions for PET imaging, for which several data sets exist as well as an IAEA evaluation based on them (red points in Fig. 1). Due to the absence of experimental data for some reactions and the large

* Corresponding author. Dept. de Física Atómica, Molecular y Nuclear. Universidad de Sevilla, Avda. Reina Mercedes s/n, Seville, 41012, Spain.
E-mail address: cguerrero4@us.es (C. Guerrero).
[1] Dept. de Física Atómica, Molecular y Nuclear. Universidad de Sevilla. Avda. Reina Mercedes s/n. Seville 41012. Spain.

https://doi.org/10.1016/j.radphyschem.2021.109759
Received 7 April 2021; Received in revised form 9 August 2021; Accepted 25 August 2021
Available online 25 September 2021

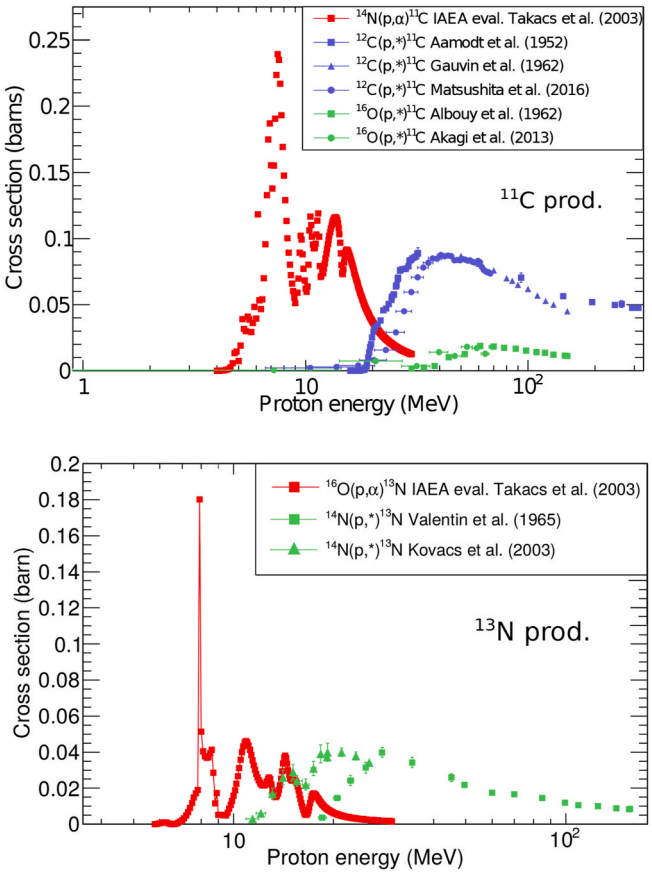

Fig. 1. Production channels of the long-lived isotopes ^{11}C (up) and ^{13}N (down) in carbon, nitrogen and oxygen, extracted from EXFOR database.

discrepancies between data sets for the ones available in EXFOR, new measurements and evaluations are required for all of these activation cross sections in the energy range of interest in proton therapy, in order to reduce the uncertainties in the estimation of the activity depth profiles and hence be able to detect beam range variations below 1 mm (Paganetti et al., 2012; Tárkányi et al., 2019; España et al., 2011).

In order to improve the current status, in this work we have developed a new technique to determine the production cross section of long-lived β^+ emitters in the full beam energy range of interest, minimizing both the number of irradiations and the systematic errors. This is done by combining the irradiation of multi-foil assembly with the measurement of the individual foils using a PET scanner. The method has been applied to the region below 18 MeV, i.e. the Bragg peak, where there is an IAEA evaluation for the reactions involved.

2. Experiments

2.1. A new approach: multi-foil activation followed by PET mapping of the individual foils

In order to cover the full energy range of interest, obtaining differential cross sections without having to perform one irradiation per energy value, a new method has been developed. As in multi-foil activation experiments, a target made as an assembly of thin foils is irradiated in such a way that the beam features a different energy as it traverses each of the foils. The novelty of the method consists in the subsequent measurement of the activity induced in all the foils individually but simultaneously, by using a PET scanner as sketched in Fig. 2. Inside the scanner, the foils are embedded in a matrix of polyethylene that serves as a converter for the positrons into 511 keV annihilation photons in the vicinity of each foil. As all the foils are measured simultaneously, this requires just a single irradiation; hence minimizing the errors associated to reproducibility of the irradiation parameters as well as the irradiation and measuring times, which are scarce and expensive, especially with clinical beams. In addition, the method overcomes the limited spatial resolution of the PET scanners (~mm), as the foils can be as thin and close to each other as needed.

In this work we have applied the proposed method to the production of ^{11}C and ^{13}N on carbon, nitrogen and oxygen below 18 MeV, using the ^{63}Zn production in Cu (IAEA standard cross section) as reference (Hermanne et al., 2018). Being this the first time that this method is used, we have validated the results by measuring the thick target production of ^{13}N in oxygen and ^{11}C in nitrogen with a conventional γ-ray detection system.

2.2. Irradiations at the CNA 18 MeV cyclotron

The IBA Cyclone 18/9 MeV installed at the Centro Nacional de Aceleradores (CNA) in Seville (Spain) is primarily used for radioisotope production for PET diagnostic. It is also coupled to an external beam line where physics experiments are carried out. The end of the beam line is closed by a 125 μm thick Mylar window and the irradiations are performed in air.

In this experiment we have irradiated polyethylene (PE), Nylon-6

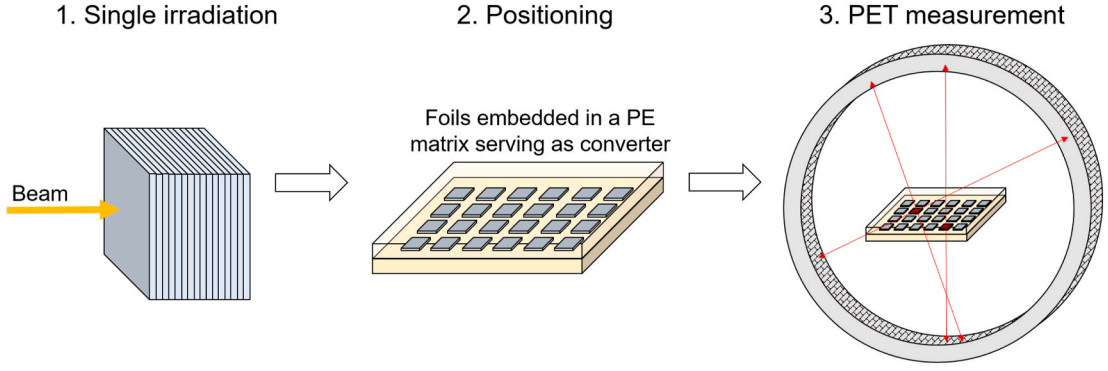

Fig. 2. Step by step of the proposed experimental method: (1) single irradiation of a target assembly of thin foils, (2) positioning of the thin films in a polyethylene matrix, (3) activity measurement with a PET scanner.

and Poly(methyl-methacrylate) (PMMA) to study the reactions producing ^{11}C and ^{13}N in carbon, nitrogen and oxygen, respectively. For each material, a stack made of a certain number of thin foils was assembled, choosing the total thickness to be slightly smaller than the corresponding beam range so that the protons traverse the targets and exit with an energy just below the corresponding reaction threshold, hitting the 2 mm graphite beam dump where the current is measured using a Brookhaven 1000c current integrator. The optimal thicknesses and the beam energy degradation along the target assembly have been calculated via SRIM-2008 (Ziegler, 1988) and Geant4 (Allison et al., 2016) simulations, which gave compatible results. The characteristics of the targets are summarized in detail in Table 1.

All the targets are mounted on a holder (see Fig. 3) coupled to a motorized table that allows placing the targets of different materials in the beam without entering the experimental room. In this way the time span between the irradiation of the different targets is minimized, and so is the decay of the activity between the irradiations and the PET measurement. In front of each assembly there are 55 mm of air and a 175 μm thick PMMA foil used for monitoring purposes: the activity induced in each of the monitor foils must be proportional to the current integrated on the beam dump for each measurement.

The energy of the protons in the interstice between the foils has been calculated with Geant4, including the 125 μm thick Mylar vacuum window, 55 mm of air and the 175 μm PMMA monitor film before each target. A gaussian fit has been done for each one of these proton energy distributions, extracting the parameters of the fit (mean value and standard deviation).

The proton energy distribution inside each foil has been calculated taking into account the distributions at the entry and the exit of each one of the foils. Then, considering an initial proton energy distribution:

$$P_i(E) = F(E, a_i) \tag{1}$$

and a final proton energy distribution:

$$P_f(E) = F(E, a_f) \tag{2}$$

where F is a gaussian function and a_i and a_f are its parameters, we can extend the proton energy distribution in function of the depth z as:

$$P_z(E) = F(E, a_z) \tag{3}$$

where the parameters a_z depends linearly on z. The average probability distribution inside the foil is calculated as:

$$P(E) = \frac{\int_{z_i}^{z_f} F(E, a_z) \cdot dz}{z_f - z_i} \tag{4}$$

The result is shown in Fig. 4. The proton energy in each foil is then defined as the mean value of the corresponding $P(E)$ distribution, with an asymmetric energy spread calculated as the point in which the

Fig. 3. Irradiation experimental setup.

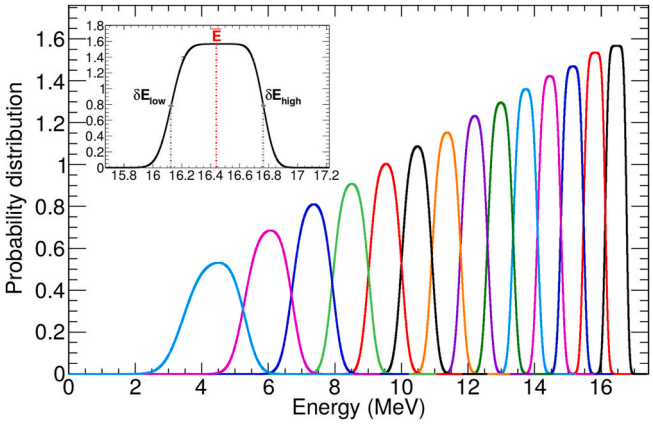

Fig. 4. Proton energy distribution after traversing each nylon-6 foil. The red curve corresponds to the energy distribution, entering the first foil, after traversing the PMMA monitor film. Inset: detailed view illustrating the calculation of the energy and spread of the beam in each target.

Table 1
Detailed information of the multi-foil target assemblies irradiated at the 18 MeV CNA cyclotron.

Material	ρ (g/cm^3)	Composition	# foils	Thickness (mm)		Range (mm E_p = 16.7 MeV	Main reactions[a]
				foil	total		
PE	0.96	C_2H_4	15	0.198(2)	2.97(3)	3.03	$^{12}C(p,pn)^{11}C$, $^{12}C(p,\gamma)^{13}N$
PMMA	1.18	$C_5O_2H_5$	14	0.171(2)	2.39(3)	2.36	$^{16}O(p,3p3n)^{11}C$, $^{16}O(\mathbf{p,\alpha})^{13}N$
Nylon-6	1.13	$C_6H_{11}NO$	14	0.183(5)	2.56(7)	2.67	$^{14}N(\mathbf{p,\alpha})^{11}C$, $^{14}N(p,pn)^{13}N$
Copper	8.92	Cu	8	0.068(1)	0.544(8)	0.586	$^{63}Cu(p,n)^{63}Zn$ (monitor)

[a] In bold the main reactions for the production of ^{11}C and ^{13}N below 18 MeV and the monitor reaction.

Table 2
Details of the performed irradiations at CNA.

Target	Irradiation for differential cross sections (detection with PET scanner)				Irradiation for validation/normalization (detection with single scintillators)			
	Current[a] (nA)	Duration (s)	Number of protons (x10^{13})	c_{decay} (%) (isotope of interest)	Current[a] (nA)	Duration (s)	Number of protons (x10^{11})	c_{decay} (%) (isotope of interest)
PE	33.8(16)	300(1)	6.3(3)	15.63(5) (^{13}N) 8.18(3) (^{11}C)	–	–	–	–
PMMA	15.9(8)	420(1)	4.17(20)	20.95(5) (^{13}N) 11.20(3) (^{11}C)	2.17(11)	48(1)	6.4(3)	2.75(6) (^{13}N) 1.37(3) (^{11}C)
Nylon-6	33.4(16)	300(1)	6.3(3)	15.63(5) (^{13}N) 8.18(3) (^{11}C)	2.15(11)	176(1)	23.7(12)	9.60(5) (^{13}N) 4.91(3) (^{11}C)
^{nat}Cu	–	–	–	–	2.37(12)	31(1)	4.59(23)	0.464(15) (^{63}Zn)

[a] The current integrator was calibrated from the results of the integral activity of ^{63}Zn induced in the copper target (see section 3.2).

probability function reaches half maximum (see inset of Fig. 4).

Apart from the irradiation carried out corresponding to the determination of the differential cross sections, another irradiation of thick PMMA, Nylon-6 and ^{nat}Cu targets was carried out for validation and normalization purposes: the resulting activity from a simplified set-up of single $LaBr_3$ and NaI detectors serves to validate the PET measurement and normalize the production yields to the ^{63}Cu(p, n)^{63}Zn standard cross section, respectively (see sections 3.2 and 3.3).

The details of each irradiation (duration, current, accumulated charge and fraction of isotopes that decay during the irradiation) are summarized in Table 2. In all cases the current was low enough to prevent damaging the targets and the length of the irradiations was chosen to produce enough activity in each target, but within the radioprotection limits of the facility. Following the irradiation, and after the approximate 20 min needed to access the experimental area, the targets were transported to the measuring stations at the PET/CT room and the detector laboratory at CNA to measure the differential and integral production yields, respectively.

2.3. Activity measurement with the PET/CT scanner

The key for measuring the cross sections as a function of the proton energy is being able to determine the activity induced in each of the foils in the corresponding assembly. The novelty in this work is that all the activated foils are studied simultaneously with the PET scanner, in this case a Siemens Biograph mCT.

A total of 46 foils from the PE, PMMA, Nylon-6 targets and PMMA monitor foils were inserted into the polyethylene matrix, forming two layers as illustrated in Fig. 5. The matrix served both to position the foils inside the scanner and to ensure the annihilation of the positrons in the vicinity of each foil: the range of the <0.96 and < 1.2 MeV positrons

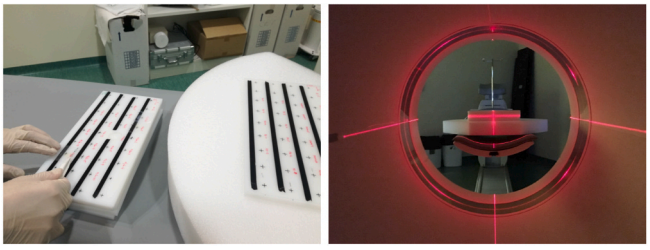

Fig. 5. Left: Positioning of the irradiated foils between the polyethylene (PE) thick layers. Right: PET measurement of the activity of the irradiated foils embedded in the PE matrix.

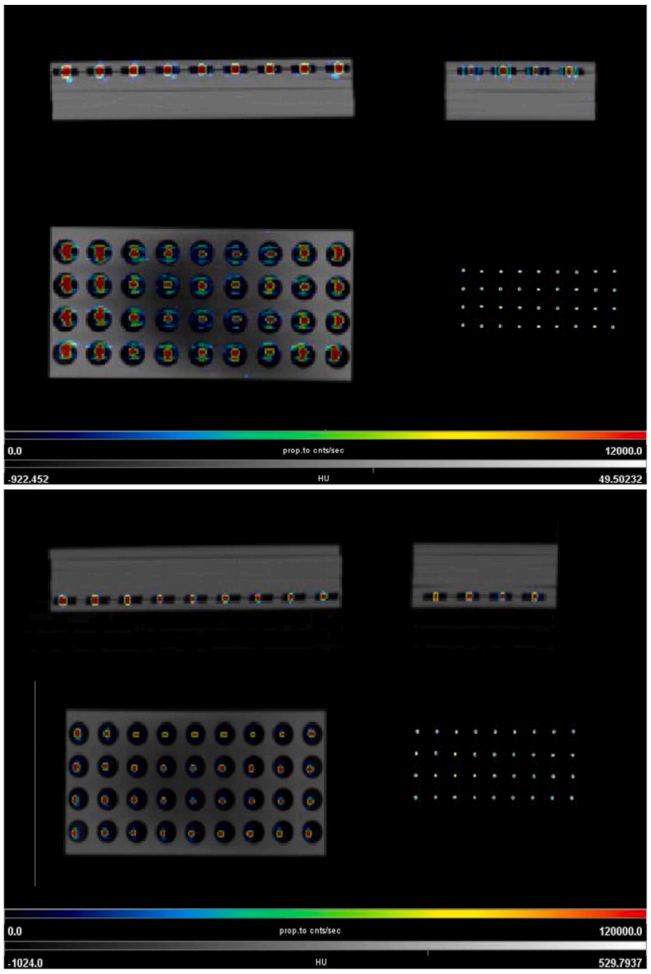

Fig. 6. Axial, sagittal and coronal PET/CT image of the two planes of the polyethylene matrix with the foils in their corresponding positions.

emitted by ^{11}C and ^{13}N is only 5 and 6 mm in polyethylene, respectively, compared to more than 4 and 8 m in air.

The PET scanner was operated in dynamic mode recording 60 s interval acquisitions during 5 h, although in 2 h the signal was already very close to the background level, as the half-lives of ^{11}C and ^{13}N are

20.36 and 9.97 min, respectively. The images are reconstructed with the TrueX with Time-Of-Flight algorithm, using a gaussian filter of 1 mm FWHM. The images obtained include the corresponding attenuation corrections according to the CT image, on top of which the PET image is displayed in Fig. 6. After identifying each foil in the PET image, the corresponding Volumes-of-Interest (VOI) are defined (spheres of 16 mm radius) and the number of counts (given by the PMOD software (Image processing software v.4.203, 2020) in units of *propcps*, i.e. proportional to counts-per-second) within each VOI is recorded as a function of time, resulting in a decay curve corresponding to each foil. The calibration from *propcps* to activity units was achieved by measuring inside the matrix a 120.8(24) kBq ^{22}Na source. An efficiency map of the scanner was made by placing the source at each one of the foil positions, evidencing relative variations between the center and the edges of the field of view smaller than 2%.

3. Data analysis

The data analysis consists in the determination of the production yields and the corresponding cross sections of interest from the activity induced during the irradiation of the individual foils measured with the PET scanner, and also in that from the activity induced during the irradiation of the ^{nat}Cu, PMMA and Nylon-6 stacks measured with the stand-alone scintillator detectors.

In all cases the measured quantity is the counting rate as a function of time, which is converted into an activity decay curve $A(t)$ by dividing it by the efficiency of each detection system (PET or conventional detectors) and the intensity associated to the decay: 0.99750(13) for ^{11}C and 0.99818(13) for ^{13}N (Bé et al., 2004). The corresponding activity value at t = 0, i.e. at the end of the bombardment A^{EOB}, is determined by fitting it to the expected exponential decay:

$$A(t) = C + A^{EOB}_{^{11}C} e^{-\lambda_{^{11}C} t} + A^{EOB}_{^{13}N} e^{-\lambda_{^{13}N} t}, \tag{5}$$

The production yield Y (activity per unit incident charge) in each target is then calculated as:

$$Y = \frac{A^{EOB}}{I_p \cdot t_{irr}} \left(\frac{\lambda t_{irr}}{1 - e^{-\lambda t_{irr}}} \right) = \frac{A^{EOB}}{I_p \cdot t_{irr}} \left(\frac{1}{1 - c_{decay}} \right) \tag{6}$$

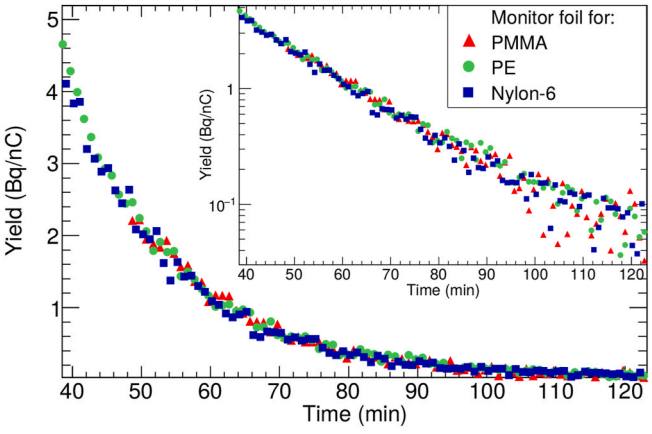

Fig. 7. Activity distribution for the PMMA monitor films placed before each stack of foils.

where I_p is the proton beam current (see Section 3.2) and t_{irr} is the irradiation time, with the second term between brackets accounting for the fraction of nuclei that decayed during the irradiation (c_{decay} is denoted in Table 2). In the case of the multi-foil target, the thin target approximation (Knoll and Kraner, 1981) allows determining the production cross section, at the energy E_i of the beam traversing foil i, from the corresponding yield Y_i as:

$$\sigma(E_i) = \frac{Y_i(E_i)}{\lambda \cdot n_i} = \frac{A^{EOB}}{I_p \cdot t_{irr} \cdot \lambda \cdot n_i} \left(\frac{1}{1 - c_{decay}} \right) \tag{7}$$

where λ is the corresponding decay constant and n_i is the areal density of foil i in units of atoms per barn.

3.1. Analysis of the activity curves from the PET scanner

The activity of the 46 irradiated foils was measured with the PET scanner using a 60 s dynamic protocol for 5 h. As mentioned in section 2.2, the first foil in each stack is a PMMA one used for monitoring and validation purposes. The activity curves of the monitoring foils, normalized to the incident charge corresponding to each irradiation are displayed in Fig. 7. The corresponding A^{EOB} values agree within 4.5%, which is then considered the uncertainty related to the reproducibility of the irradiations.

The decay curves for a selection of Nylon-6 foils are displayed in Fig. 8 together with the corresponding fits (see Eq. (5)). The fits properly reproduce the data and indicate a negligible constant term, as expected. As mentioned before, the parameters of the fit provide the activity per unit charge just after the irradiation for each of the produced β^+ emitters. However, since PMMA and Nylon-6 contain also oxygen and nitrogen, different reaction channels contribute to the production of ^{11}C and ^{13}N. Therefore the production yield in oxygen and nitrogen were obtained, respectively, by subtracting the carbon contribution (obtained previously from the PE films) from PMMA and the carbon and oxygen contributions (obtained previously with the PMMA films) from Nylon-6. The production cross section of ^{11}C and ^{13}N in ^{12}C, ^{16}O and ^{14}N can be written as:

$$\sigma_{j \to i} = \frac{A^{EOB}_i}{I_p \cdot t_{irr} \cdot \lambda_i \cdot p_j \cdot n_j} - \sum_{k(k \neq j)} \frac{n_k \cdot \sigma_{k \to i}}{p_j \cdot n_j} \tag{8}$$

where i stands for the produced isotope (^{11}C and ^{13}N), main (j) and other (k) stand for the isotopes from which i can be produced, $n_{j(k)}$ is the number of atoms of the isotope j(k) in each target per barn and p_j is the isotopic relative abundance.

The subtraction term in Eq. (8) depends on each case:

- ^{12}C(p,*): nothing needs to be subtracted.
- ^{16}O(p,3p3n)^{11}C: only carbon contribution. The subtraction term is lower than 1%, as the production in carbon is negligible.
- ^{16}O(p,α)^{13}N: only carbon contribution. The subtraction term ranges between 3% and 9%, except below 7.7(6) MeV, where it is increased up to 24%.
- ^{14}N(p,α)^{11}C: only oxygen contribution, as the carbon contribution is negligible. The subtraction term is lower than 2%.
- ^{14}N(p,pn)^{13}N: subtraction term becomes very important (>70%) at all energies, due to the oxygen contribution (carbon contribution is negligible). Therefore, this reaction is not considered in this work.

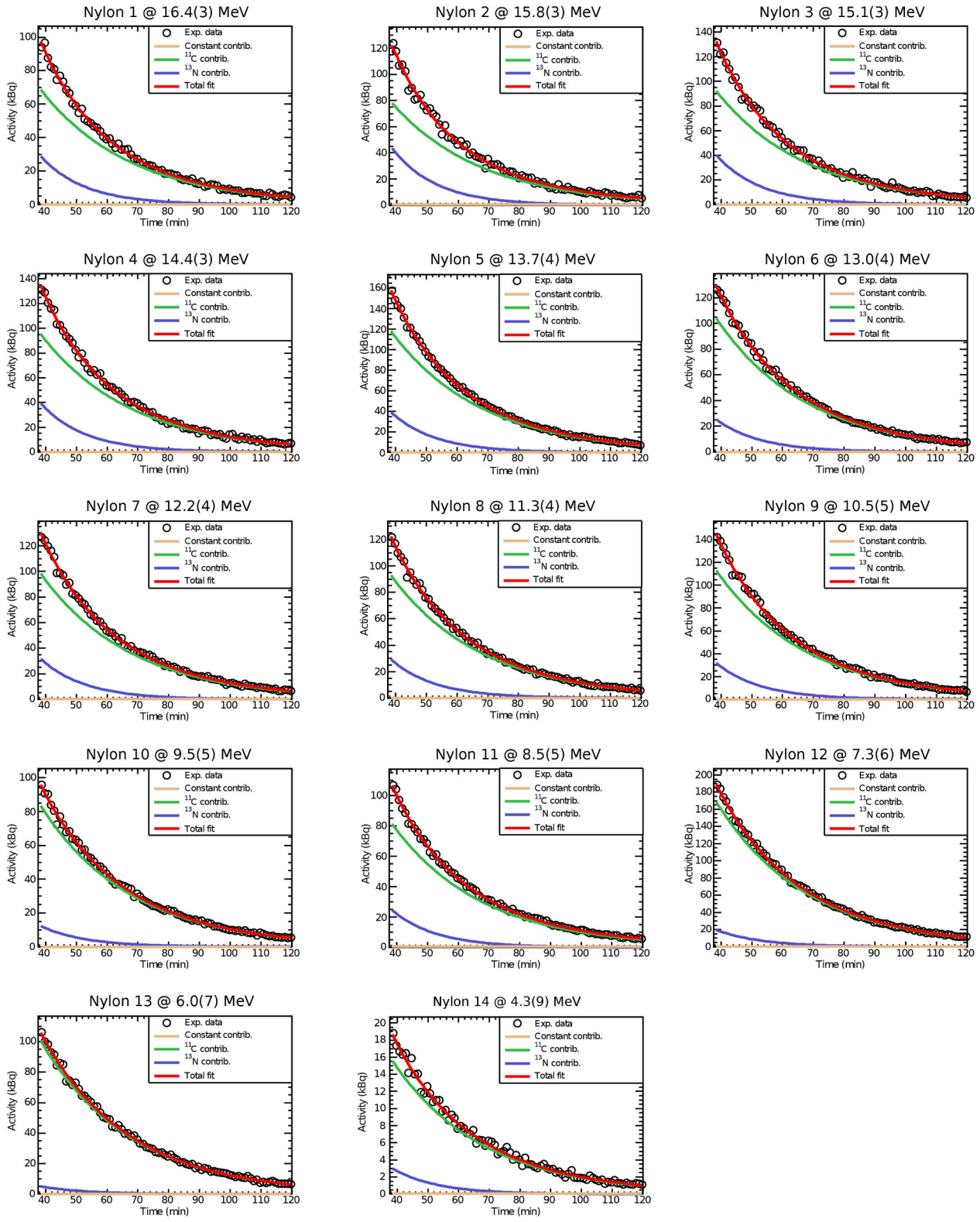

Fig. 8. Activity curve for the 511 keV emission in the Nylon-6 targets (for a proton energy from 16.4(4) MeV to 4.3(15) MeV). The decay curves are fit up to 5 h, although the background level is reached in 2 h. The curves start at 40 min because it is the time span between the end of the irradiation of Nylon-6 and the start of the PET measurement.

Table 3
Details of the γ-ray decay lines from ^{63}Zn studied together with the experimental and IAEA reference productions yields.

E_γ(keV)	I_γ(%)	ϵ(%)	Yield (kBq/nC)	Y_{IAEA} (kBq/nC)
511	185.6(9)	0.217(3)	2.24(11)	
670	8.19(32)	0.1773(14)	2.31(11)	2.01(8)
962	6.50(16)	0.1284(18)	2.24(11)	

3.2. Normalization to the reference ^{63}Cu(p,n)^{63}Zn cross section

The IAEA has recently published an evaluated data set for monitor reactions induced by charged particles (Hermanne et al., 2018). In this work, the ^{63}Cu(p, n)^{63}Zn reaction has been used as reference, with the β^+ emitter ^{63}Zn featuring a half-life of 38.47(5) min. A natural Cu target (2 mm thick) was irradiated (see Table 1) and the induced activity measured with a 1,5″×1,5″ $LaBr_3$ detector, which efficiency curve was determined from ^{137}Cs and ^{22}Na γ-ray sources and a Geant4 Monte Carlo simulation (which indicated that the $LaBr_3$ crystal size is actually 1.44″×1.44″). The irradiated Cu target was sandwiched between a pair of 2 mm thick lead foils acting as positron converters and placed at 100 mm from the front face of the detector.

Three γ-ray decay lines were studied: 511, 670 and 962 keV. As illustrated in Table 3, the ^{63}Zn production yields from the 3 lines are compatible within 1.7%, proving the accuracy of the attenuation and efficiency corrections for the three energies. The reported 4.8% uncertainty includes that of the activity curve fit (~0.5%), the efficiency (<1.4%, see Table 3), the uncertainty in the Monte Carlo corrections to consider the differences in efficiency between a extensive positron emitter (^{63}Zn) and a punctual ^{22}Na calibration source (~0.6%) and the reproducibility of the measurements (4.5%, see Section 3.1).

The thick target physical yield of the IAEA evaluation for ^{63}Cu(p, n)^{63}Zn for 16.7 MeV protons is 2.01(8) kBq/nC. The comparison with the experimental value of 2.24(10) kBq/nC from the ^{63}Zn 511 keV line indicates that normalizing to the IAEA monitor reaction requires scaling down the measured values by 10%, and that was done for the values reported below.

Table 4
Experimental production cross sections for the ^{14}N(p,α)^{11}C reaction. The last column shows the IAEA cross section integrated in each energy range.

E_p (MeV)	This work	IAEA eval. (Takacs, 2003)
	σ (mb)	σ (mb)
16.4(3)	70(5)	95(5)
15.8(3)	81(7)	93(5)
15.1(3)	96(8)	102(5)
14.4(3)	99(9)	99(5)
13.7(4)	123(9)	139(7)
13.0(4)	108(8)	110(5)
12.2(4)	102(8)	91(5)
11.3(4)	96(7)	108(5)
10.5(5)	117(9)	98(5)
9.5(5)	86(7)	83(4)
8.5(5)	84(7)	100(5)
7.3(6)	175(14)	196(10)
6.0(7)	103(8)	66(3)
$4.3^{+0.9}_{-1.0}$	14.4(13)	8.0(4)

Table 5
Experimental production cross sections for the ^{16}O(p,3p3n)^{11}C and ^{16}O(p,α)^{13}N reactions. The last column shows the IAEA cross section integrated in each energy range.

E_p (MeV)	This work		IAEA eval. (Takacs, 2003)
	σ (mb)		σ (mb)
	^{16}O(p,3p3n)^{11}C	^{16}O(p,α)^{13}N	^{16}O(p,α)^{13}N
16.4(3)	0	9.8(8)	8.7(16)
15.8(3)	0.54(13)	19.3(15)	18(3)
15.2(3)	0.52(15)	34(3)	29(6)
14.5(3)	0.73(16)	42(3)	38(7)
13.8(4)	0.3(6)	48(4)	26(5)
13.1(4)	0.67(22)	27.9(22)	21(4)
12.3(4)	0.6(3)	35(3)	26(5)
11.5(4)	0.88(23)	40(3)	36(7)
10.7(4)	1.5(3)	59(5)	44(8)
9.8(5)	1.54(22)	24.3(19)	12.5(23)
8.8(5)	1.46(20)	13.0(10)	25(5)
7.7(6)	1.9(3)	36(3)	36(7)
6.5(7)	1.85(20)	0.63(7)	1.06(20)
5.0(8)	1.88(21)	0	0.09(17)

Table 6
Experimental production cross sections for the ^{12}C(p,pn)^{11}C and ^{12}C(p,γ)^{13}N reactions.

E_p (MeV)	σ (mb)	
	^{12}C(p,pn)^{11}C	^{12}C(p,γ)^{13}N
16.4(3)	0.29(3)	0.69(7)
15.8(3)	0	0.46(4)
15.1(3)	0	0.45(6)
14.4(4)	0	0.47(4)
13.7(4)	0	0.56(4)
12.9(4)	0	0.54(4)
12.2(4)	0	0.60(5)
11.3(4)	0	0.56(4)
10.4(5)	0	0.74(6)
9.5(5)	0	0.88(7)
8.4(6)	0	1.41(11)
7.2(6)	0	1.82(15)
$5.9^{+0.7}_{-0.8}$	0	2.09(17)
4.2(10)	0	1.89(15)
2.0(12)	0	0.79(6)

3.3. Validation of the PET scanner with conventional detectors

Being this the first time that the PET scanner is used for measuring absolute activity values, a validation by comparing the results with a conventional detection system was made. For this purpose, two targets of PMMA and Nylon-6 with the same thickness than that of the envisaged target assembly used for the PET measurement (see Table 1) were irradiated under the same conditions. Then the activity produced in the thick targets was measured with a NaI and $LaBr_3$ detectors, respectively, in a configuration similar to the one discussed in the previous section.

The production yields of the Nylon-6, PMMA and PE assemblies from PET measurement are listed, respectively, in Tables A.7, A.8 and A.9 in Appendix, together with the result from the integral measurement with the stand-alone scintillator for the Nylon-6 and PMMA assemblies (see Table A.7 and A.8, respectively, in Appendix). In the case of Nylon-6, the production of ^{11}C was determined as 502(17) Bq/nC. The corresponding value from the PET measurement, obtained as the sum of the activities of each one of the individual foils (see Table A.7 in Appendix), amounts to

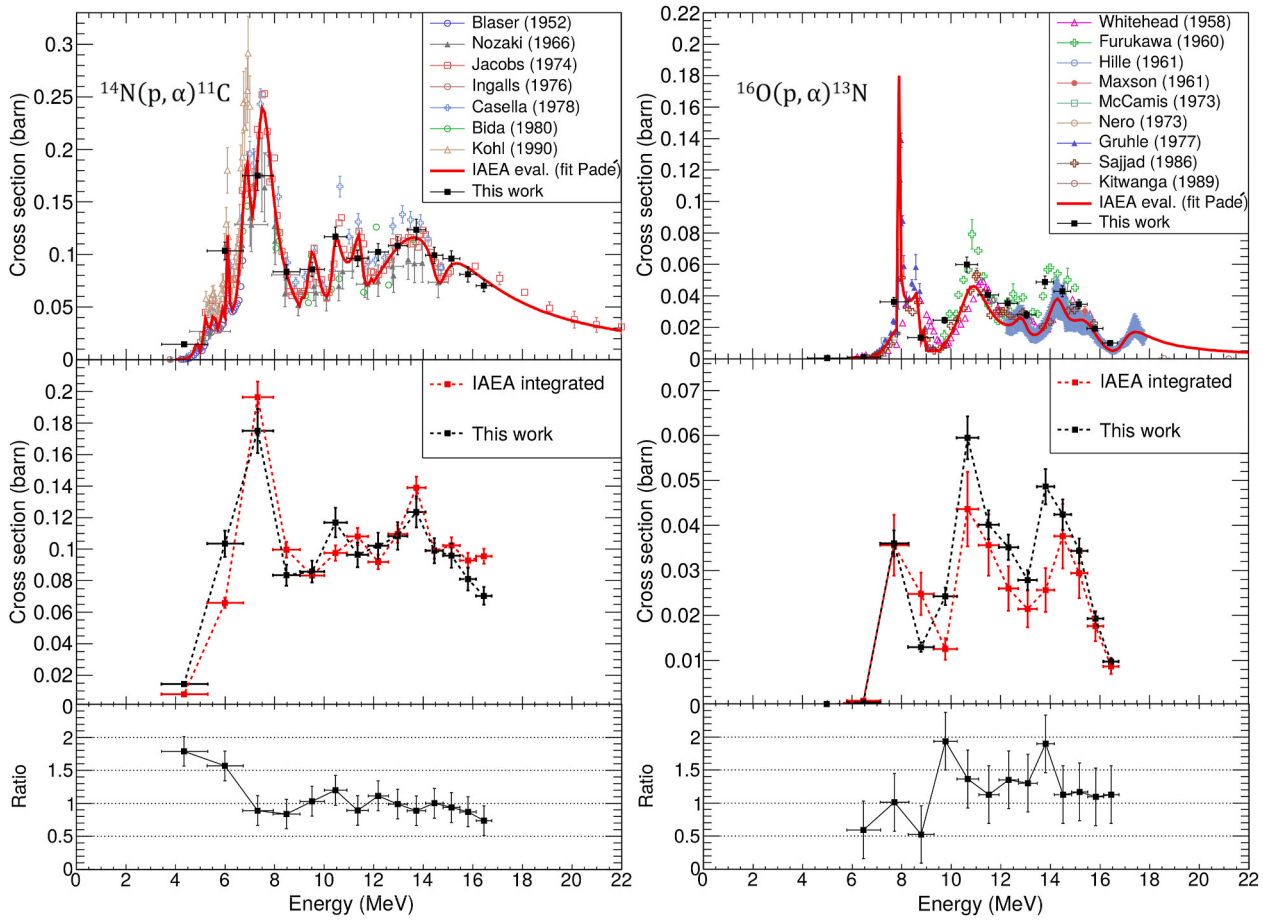

Fig. 9. Top: Selected data for the IAEA evaluation and recommended parametrization (fit Padé) for ^{14}N(p,α)^{11}C (left) and ^{16}O(p,α)^{13}N (right) reactions. Middle: Experimental and evaluated data integrated in the energy intervals of our measurement for ^{14}N(p,α)^{11}C (left) and ^{16}O(p,α)^{13}N (right). Bottom: Ratios of the obtained data sets with respect the evaluation for ^{14}N(p,α)^{11}C (left) and ^{16}O(p,α)^{13}N (right).

520(30). In the case of PMMA, the integral production of ^{13}N was determined as 709(23) Bq/nC, and the corresponding value from the PET measurement as 760(40) Bq/nC.

Both PET measurements are in agreement with the value from the thick target within 4% and 6%, respectively. The average deviation of the integral and PET measurement (5%) is assumed by the uncertainty related to the reproducibility of the irradiations (see Section 3.1), hence validating the use of a PET scanner as a detector capable of making accurate absolute activity measurements. This is remarkable considering that the attenuation corrections are very different in both set-ups: 2 mm of lead in the stand-alone scintillator detector case (accounted for via Geant4 simulations) vs. several centimetres of polyethylene plus the bed in the PET scanner (accounted for the PET reconstruction software using the corresponding CT image).

4. Results

The production yields of ^{11}C and ^{13}N in each of the foils of different materials are summarized in the Appendix in Tables A.7, A.8 and A.9. From these values the cross sections for the different reactions have been extracted using Eq. (8). The results are summarized in Tables 4–6, together with the reference values of Takacs et al. corresponding to the IAEA evaluation (IAEA, 2001) for the reactions ^{14}N(p,α)^{11}C and ^{16}O(p,α)^{13}N. The uncertainty of the measured cross sections has contributions from the fit (given by ROOT (Root data analysis framework v.5.34.30, 2015)), the spatial dependence of the PET scanner efficiency (2%), the activity of the ^{22}Na calibration source (2%), the uncertainty in the foil thickness (1%), the accuracy of the current integrator (5%) and the subtraction of the competing reactions (see Section 3.1). The best accuracy reached amounts to ~6%.

4.1. Comparison to previous data and the IAEA recommended values

In 2001, an evaluation was elaborated in the framework of an IAEA project (IAEA, 2001) for ten reactions resulting in positron emitters of interest for medical radioisotope production, including the reactions ^{14}N(p,α)^{11}C and ^{16}O(p,α)^{13}N studied in this work.

^{14}N(*p,α*)^{11}C

The IAEA evaluation is based on nine of the thirteen data sets available in EXFOR in the region between 4 and 25 MeV: Blaser et al. (1952), Nozaki et al. (three data sets) (Nozaki et al., 1966), Jacobs et al.

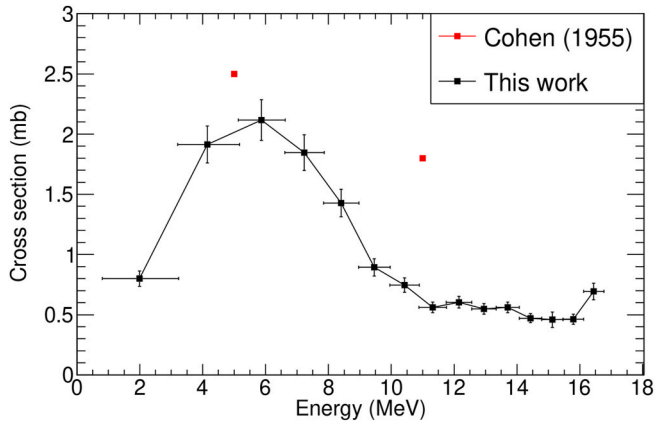

Fig. 10. Experimental cross section for the $^{12}C(p,\gamma)^{13}N$ reaction.

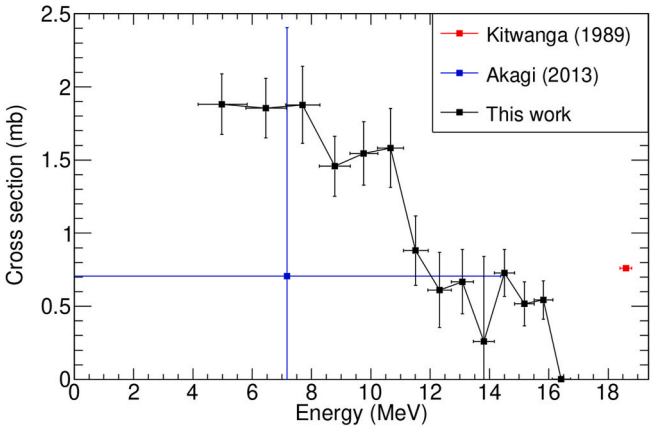

Fig. 11. Experimental cross section for the $^{16}O(p,3p3n)^{11}C$ reaction.

(1974), Ingalls et al. (1976), Casella et al. (1978), Bida et al. (1980) and Köhl et al. (1990). The deviations of the selected data from the evaluation are on average about 5%. In order to have better agreement with the other data sets, the values of Köhl et al. were arbitrarily divided by a factor of 1.4. For the same reason, the values of Blaser et al. were multiplied by a factor of 1.3 and uniformly shifted by −0.7 MeV to reproduce the resonances. Several data points of Bida et al. were removed to allow a better fitting of the resonances at low energy (4 low energy points and a point at 12.2 MeV removed). These data sets were used as input for a least-squares Padé fit with 75 parameters and 306 selected data points with a $\chi^2 = 3.61$. The uncertainties of the fit range between 60% around 5 MeV, decrease to below 8% between 13 and 28 MeV and rise again to 10% at the highest energy (Hermanne et al., 2020). The evaluation is displayed in the top panel of Fig. 9 together with the individual unmodified data sets and the results of this work. After the mentioned modifications, the deviations of the selected data sets from the evaluation are on average 4%, which we consider as the uncertainty bars for this IAEA evaluation curve in Fig. 9.

Our measurement reproduces the resonance structure quite well, even with the limited resolution of our method at low energies, i.e. at the very end of the proton range. However, this graphical representation can be misleading in the sense that the experimental data (in particular in this work) are integrated over an energy interval corresponding to the proton energies in each thin foil. These energy intervals are illustrated as error bars in the energy axis; hence they cannot be directly compared with the analytical curve of the evaluation. Therefore, the evaluation has been integrated in the energy intervals defined by our data points, resulting in the values displayed in the middle panel of Fig. 9 (left). The cross section ratios displayed in the bottom panel of Fig. 9 (left) illustrate the good agreement of our data and the evaluation, with sizable discrepancies only in the two data points corresponding to the low energy tail of the resonance, which might be due to the limited resolution of our measurement at such low energies. But these two points account for very little in the overall picture because the cross section there is low. On average, considering the ratio weighted by the cross section value, the agreement between our results and the evaluation is a remarkable 2%.

$^{16}O(p,\alpha)^{13}N$

In this case, the evaluation is based in ten of the fourteen data sets available up to 35 MeV. The evaluation included the data of Whitehead and Foster (1958), Furukawa et al. (1960), Hille et al. (1961), Maxson (1961), Dangle et al. (1964), McCamis et al. (1973), Nero and Howard (1973), Gruhle and Kober (1977), Sajjad et al. (1986) and Kitwanga et al. (1989). The deviations of the selected data from the evaluation are on average about 19%. In order to have better agreement with other data sets, the original data of Furukawa et al. were multiplied by a factor of 0.7, and the data of Whitehead et al. were shifted to lower energies by 0.3 MeV to reproduce the resonances. The data of Dangle et al. is not available at EXFOR database. These data sets were used as input for a least-squares Padé fit with 40 parameters and 607 selected data points with a $\chi^2 = 1.96$. The uncertainties of the fit range between 65% near the reaction threshold, decrease to below 7% between 11 and 18 MeV and then monotonically increase to reach 12% at the highest energy (Hermanne et al., 2020). The evaluation and the data are illustrated in Fig. 9, together with the results of this work. In this case, after the mentioned modifications, the deviations of the selected data sets from the evaluation are on average 14%, which we consider the uncertainty bars for this IAEA evaluation curve in Fig. 9 as well.

As in the case of the $^{14}N(p,\alpha)^{11}C$ reaction, the evaluated cross section integrated over the energy intervals used in this work and the corresponding cross section ratios are displayed in the middle and bottom panels of Fig. 9 (right). Our data show the first very narrow resonance structure even with the limited energy resolution of the method, which may be the cause of the slight different cross section shapes between 9 and 10 MeV. Above 10 MeV, our data are systematically larger than the evaluation, 20% considering the ratio weighted by the cross section. This difference is significant but in the order of that observed in other data sets. For instance, the original data of Furukawa Furukawa et al. (1960), Whitehead (Whitehead and Foster, 1958) and Gruhle (Gruhle and Kober, 1977) are 53%, 37% and 43% larger than the evaluation, correspondingly, sizable differences pointing in the same direction than our results: an underestimation of the evaluated cross section.

$^{12}C(p,\gamma)^{13}N$

The cross section obtained for the $^{12}C(p,\gamma)^{13}N$ reaction from 2 MeV to 16.4 MeV is displayed in Fig. 10. This production is measured by means of the activation of the polyethylene assembly, so it is unnecessary to subtract the contribution from any isotope, hence increasing the reliability of the data presented herein. The goodness of the fit process is also increased by the fact that there is no contribution from ^{11}C, as the energy threshold for producing this isotope is 17.8 MeV, and that there is a good statistic in all the foils. Fig. 10 also shows the only data available in EXFOR for this reaction: Cohen (1955), with two points

significantly above our data and without quoted uncertainties.

$^{16}O(p,3p3n)^{11}C$

The cross section obtained for the $^{16}O(p,3p3n)^{11}C$ reaction from 5 MeV to 16.4 MeV is displayed in Fig. 11, providing a new data set at this energy range, where there is nearly no data. In this case, the effect of the subtraction term is negligible, as the cross section extracted from carbon is zero (threshold of the reaction in 17.8 MeV), increasing the confidence in our results.

$^{14}N(p,pn)^{13}N$

This reaction is not considered due to the large uncertainties in the subtraction term (see Section 3.1), dominated by the $^{16}O(p,\alpha)^{13}N$ reaction. Using a Nylon-6 assembly, it was not possible to extract reliable results for this reaction at these energies, for which an oxygen-free N-rich target material is required.

5. Conclusions and outlook

Offline PET range verification in proton therapy relies on the accuracy of the production cross sections of the long-lived positron emitters ^{13}N and ^{11}C on the most abundant elements in the human body: C, N and O. In view of the need of a more accurate experimental data base for the corresponding reactions, a new technique for determining the reaction cross sections of interest has been developed and validated with measurements at the distal fall-off of the Bragg peak (below 18 MeV).

The novelty of the method is that the common multi-foil activation technique is combined with the use of a PET scanner as a detector, measuring the activity of all the foils at the same time in only one PET acquisition, hence minimizing the number of irradiations and the systematic error in the irradiation and in the following activity-induced measurement. The method has been employed to determine, among others, the production yields and cross sections of the principal reactions $^{14}N(p,\alpha)^{11}C$ and $^{16}O(p,\alpha)^{13}N$ below 18 MeV. The results indicate discrepancies with the IAEA evaluations of 2% and 20%, respectively. This method has been validated by means of two integral production yield measurements using a Nylon-6 and PMMA thick targets, conventional scintillator detectors and the standard cross section of $^{63}Cu(p,n)^{63}Zn$ for normalization purposes. The integral measurements are in good agreement with the sum of the activities of each one of the individual foils, hence validating the use of the PET scanner for this purpose. This, together with the good agreement between the measured and the evaluated cross section data for the $^{14}N(p,\alpha)^{11}C$ reaction, much more accurate than the $^{16}O(p,\alpha)^{13}N$ evaluation, shows the reliability of the data presented herein.

The method will be employed for measurements in the full energy range of interest for proton therapy (up to 230 MeV) in a clinical beam facility. In order to cover this energy range with enough energy resolution, more than one incident beam energy is needed. Indeed, the measuring plan includes three irradiations between 70 and 200 MeV. This is based on the use of 1 mm thick polyethylene, PMMA and Nylon-6 targets intercalated with polyethylene degraders. The irradiation at each energy provides results at energies that overlap with the following lower energy irradiation, in such a way that the compatibility between the results from the different irradiations can be cross-checked. As described before, the irradiated targets will then be measured with a clinical PET scanner, providing the decay activity curve of several foils in only one acquisition.

CRediT author statement

Teresa Rodríguez-González: Methodology, Software, Validation, Formal análisis, Investigation, Writing - Original Draft.

Carlos Guerrero: Conceptualization, Methodology, Formal analysis, Investigation, Resources, Writing - Review & Editing, Supervision, Project administration.

María del Carmen Jiménez-Ramos: Methodology, Investigation, Resources, Writing - Review & Editing, Supervision.

Jorge Lerendegui-Marco: Methodology, Software, Validation, Investigation.

María de los Ángeles Millán-Callado: Investigation.

Ángel Parrado: Investigation.

Joaquín Gómez: Resources, Supervision, Funding acquisition.

José Manuel Quesada: Resources, Supervision, Funding acquisition.

Declaration of competing interest

The authors declare that they have no known competing financial interests or personal relationships that could have appeared to influence the work reported in this paper.

Acknowledgments

This project has received funding from the Spanish Ministry of Economy and Competitiveness projects RYC-2014-15271, FPA2016-77689-C2-1-R and RTI2018-098117-B-C21, from the European H2020-847552 (SANDA) and the V Plan Propio de Investigación Programme from the University of Sevilla. T. Rodriguez-Gonzalez acknowledges the Spanish FPI predoctoral grant.

Appendix A

Table A.7
Experimental production yields in Nylon-6 assembly. The bottom of the table contains the integral value from both the differential and integral yields measurements with the PET and the scintillator systems, respectively.

E_p (MeV)	Yield (Bq/nC)	
	^{11}C	^{13}N
16.4(3)	27.4(14)	49(3)
15.8(3)	31.2(16)	74(4)
15.1(3)	36.9(19)	69(5)
14.4(3)	38.1(20)	67(6)

(*continued on next page*)

Table A.7 (*continued*)

E_p (MeV)	Yield (Bq/nC)	
	^{11}C	^{13}N
13.7(4)	47.4(24)	67(4)
13.0(4)	41.6(21)	43.2(22)
12.2(4)	39.3(20)	54(4)
11.3(4)	37.2(19)	50(3)
10.5(5)	45.2(23)	54(3)
9.5(5)	33.4(17)	21.1(22)
8.5(5)	32.5(17)	42(4)
7.3(6)	67(3)	34(3)
6.0(7)	40.3(20)	8.7(12)
$4.3^{+0.9}_{-1.0}$	6.2(3)	5.1(5)
<16.7 MeV (PET)	520(30)	–
<16.7 MeV ($LaBr_3$)	502(17)	–

Table A.8
Experimental production yields in PMMA assembly. The bottom of the table contains the integral value from both the differential and integral yields measurements with the PET and the scintillator systems, respectively.

E_p (MeV)	Yield (Bq/nC)	
	^{11}C	^{13}N
16.4(3)	0.32(6)	20.8(12)
15.8(3)	0.51(10)	37.1(20)
15.2(3)	0.46(10)	64(3)
14.5(3)	0.64(11)	79(4)
13.8(4)	0.23(13)	91(5)
13.1(4)	0.59(10)	53(3)
12.3(4)	0.54(10)	66(3)
11.5(4)	0.78(11)	75(4)
10.7(4)	1.40(16)	111(6)
9.8(5)	1.37(13)	48(3)
8.8(5)	1.29(12)	29.2(17)
7.7(6)	1.66(16)	73(4)
6.5(7)	1.64(13)	10.2(10)
5.0(8)	1.67(9)	0
<16.7 MeV (PET)	–	760(40)
<16.7 MeV ($LaBr_3$)	–	709(23)

Table A.9
Experimental production yields in polyethylene assembly.

E_p (MeV)	Yield (Bq/nC)	
	^{11}C	^{13}N
16.4(3)	1.29(9)	6.1(5)
15.8(3)	0	4.1(3)
15.1(3)	0	4.0(5)
14.4(4)	0	4.14(22)
13.7(4)	0	4.9(3)
12.9(4)	0	4.8(3)
12.2(4)	0	5.3(3)
11.3(4)	0	4.9(3)
10.4(5)	0	6.6(4)
9.5(5)	0	7.9(4)
8.4(6)	0	12.6(6)
7.2(6)	0	16.2(8)
$5.9^{+0.7}_{-0.8}$	0	18.6(9)
4.2(10)	0	16.8(9)
2.0(12)	0	7.0(4)

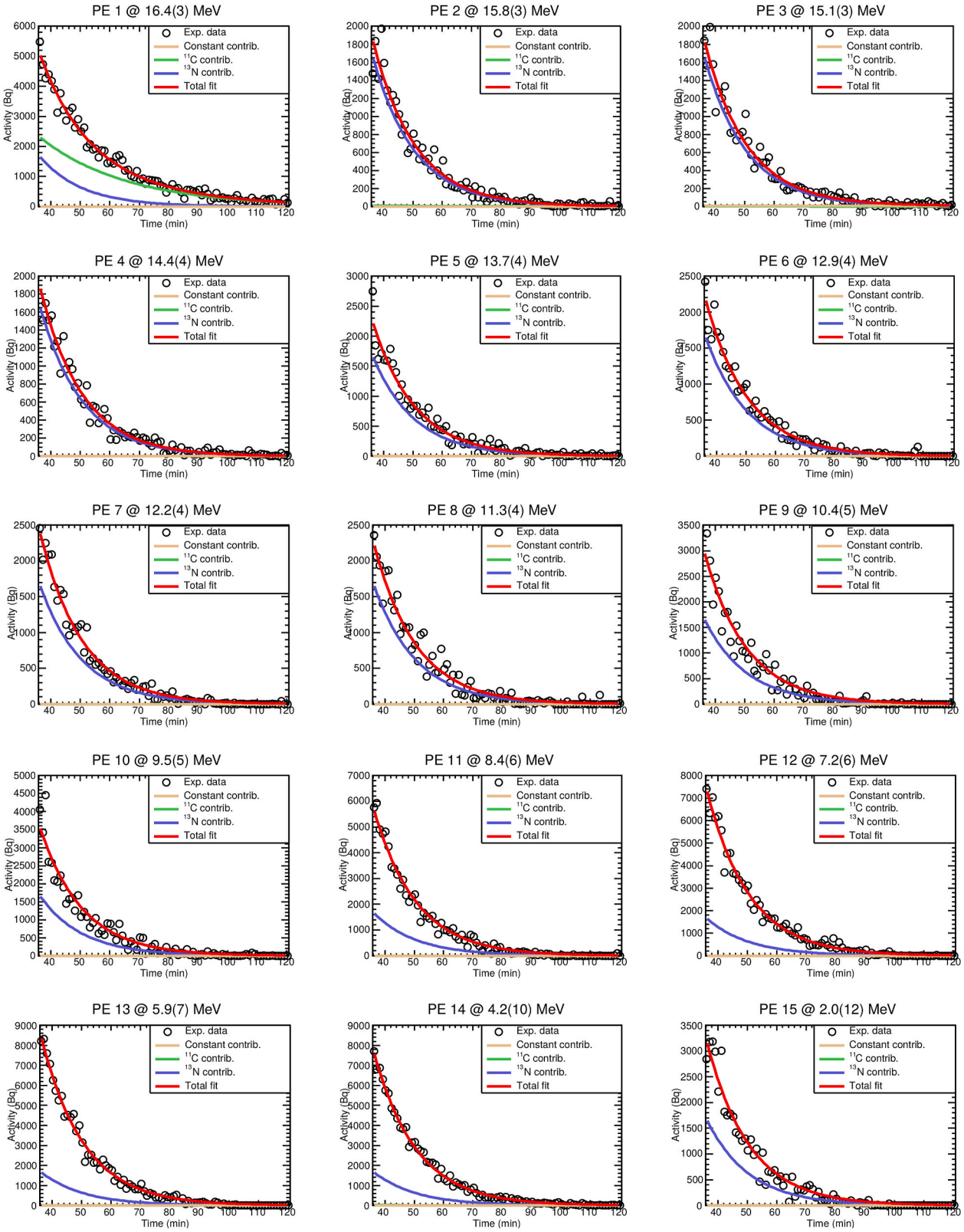

Fig. A.12. Time spectrum of the 511 keV intensity peak for the polyethylene targets. The green line shows the fit of the decay of the ^{11}C produced in polyethylene. The blue line shows the fit corresponding to the ^{13}N contribution and the red line shows the total fit (^{11}C + ^{13}N constant). The yellow line represents the background levels.

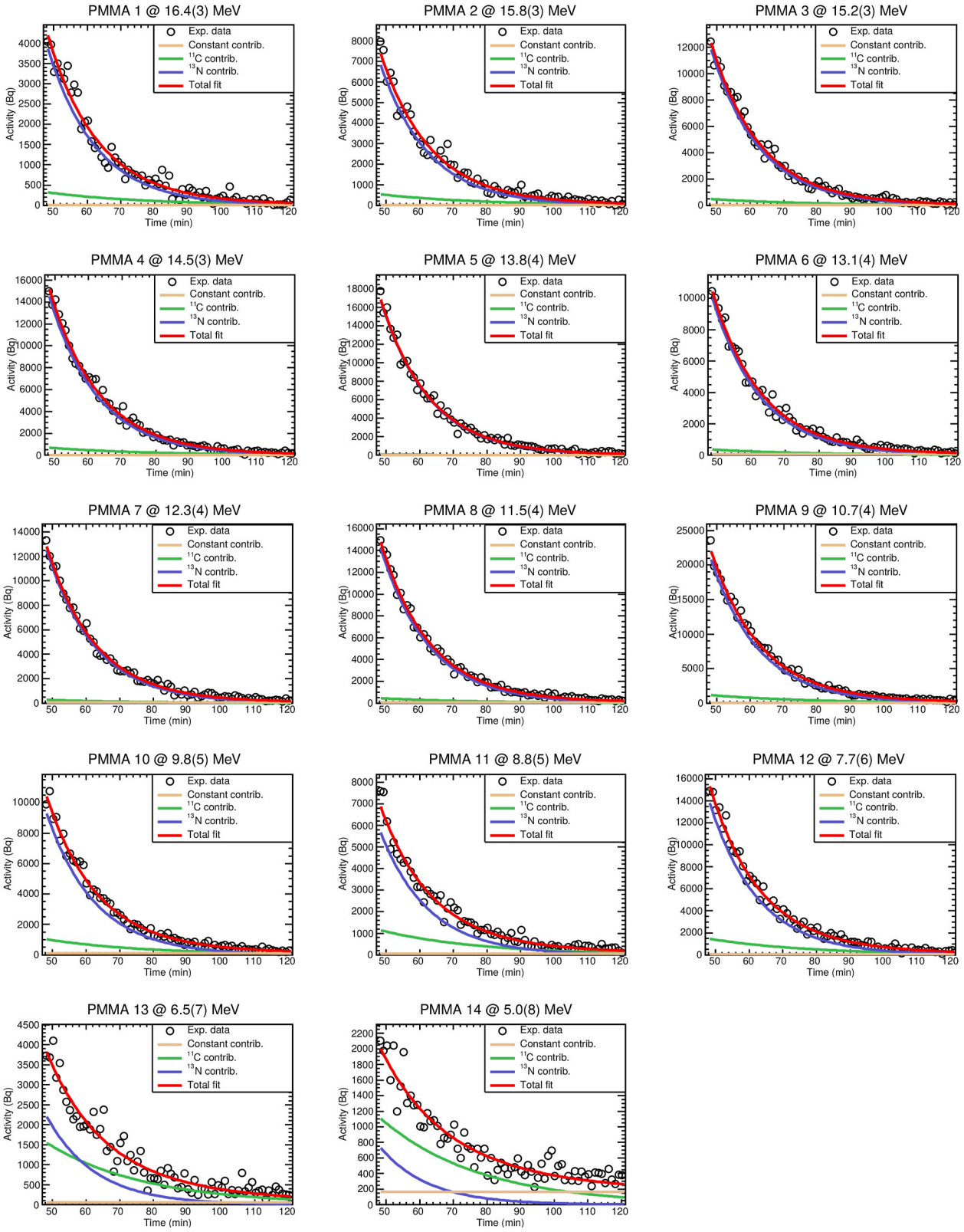

Fig. A.13. Time spectrum of the 511 keV intensity peak for the PMMA targets. The green line shows the fit of the decay of the ^{11}C produced in PMMA. The blue line shows the fit corresponding to the ^{13}N contribution and the red line shows the total fit (^{11}C + ^{13}N constant). The yellow line represents the background levels.

References

Allison, J., et al., 2016. Recent developments in Geant4. Nucl. Instrum. Methods Phys. Res. Sect. A Accel. Spectrom. Detect. Assoc. Equip. 835 https://doi.org/10.1016/j.nima.2016.06.125.

Bé, M.-M., et al., 2004. Table of Radionuclides (Vol. 1-A = 1 to 150), 1. Bureau International Des Poids Et Mesures.

Bida, G.T., Ruth, T.J., Wolf, A.P., 1980. Experimentally determined thick target yields for the ^{14}N(p,α) ^{11}C reaction. Radiochim. Acta 27. https://doi.org/10.1524/ract.1980.27.4.181.

Blaser, et al., 1952. Anregungsfunktion der kernreaktion ^{14}N(p,α) ^{11}C. Helv. Phys. Acta 25, 442.

Casella, V.R., et al., 1978. Excitation functions for the ^{14}N (p,α) ^{11}C reaction up to 15 MeV. Radiochim. Acta 25. https://doi.org/10.1524/ract.1978.25.1.17.

Cohen, B.L., 1955. (p,γ) cross sections. Phys. Rev. 100 https://doi.org/10.1103/PhysRev.100.206.

Dangle, R.L., Oppliger, L.D., Hardie, G., 1964. ^{16}O(p,α)^{13}N and ^{16}O(p,p')^{16}O differential cross-sections. Phys. Rev. 133 https://doi.org/10.1103/PhysRev.133.B647.

España, S., et al., 2011. The reliability of proton-nuclear interaction cross-section data to predict proton-induced PET images in proton therapy. Phys. Med. Biol. 56 https://doi.org/10.1088/0031-9155/56/9/003.

Furukawa, M., et al., 1960. Excitation function for the reaction ^{11}B(p,n)^{11}C up to E_p=15 MeV and energy levels of ^{12}C. J. Phys. Soc. Jpn. 15 https://doi.org/10.1143/JPSJ.15.2167.

Gruhle, W., Kober, B., 1977. The reactions ^{16}O(p,α), ^{20}Ne(p,α) and ^{24}Mg(p,α). Nucl. Phys., Sec. A 286. https://doi.org/10.1016/0375-9474(77)90601-7.

Hermanne, A., et al., 2018. Reference cross sections for charged-particle monitor reactions. Nucl. Data Sheets 148. https://doi.org/10.1016/j.nds.2018.02.009.

Hermanne, A., et al., 2020. Upgrade of IAEA recommended data of selected nuclear reactions for production of PET and SPECT isotopes. arXiv.

Hille, et al., 1961. High-resolution measurements of the^{16}O(p,α)^{13}N excitation function. Phys. Rev. 123.

IAEA, 2001. Charged Particle Cross-Section Database for Medical Radioisotope Production: Diagnostic Radioisotopes and Monitor Reactions. IAEA-Tecdoc-1211.

Image processing software v.4.203, https://www.pmod.com/web/(2020).

Ingalls, P.D., Schweitzer, J.S., Anderson, B.D., Rios, M., 1976. ^{14}N(p,α)^{11}C cross-sections from 3.8 to 6.4 MeV. Phys. Rev. C 13. https://doi.org/10.1103/PhysRevC.13.524.

Jacobs, W.W., et al., 1974. Production of Li and B in proton and alpha particle reactions on ^{14}N at low energies. Phys. Rev. C 9. https://doi.org/10.1103/PhysRevC.9.2134.

Kitwanga, S.W., et al., 1989. Production of ^{13}N radioactive nuclei from ^{13}C(p,n) or ^{16}O (p,α) reactions. Phys. Rev. C 40. https://doi.org/10.1103/PhysRevC.40.35.

Knoll, G.F., Kraner, H.W., 1981. Radiation Detection and Measurement, 69. https://doi.org/10.1109/PROC.1981.12016.

Knopf, A.C., Lomax, A., 2013. In vivo proton range verification: A review. Phys. Med. Biol. 58 https://doi.org/10.1088/0031-9155/58/15/R131.

Köhl, F., et al., 1990. Determination of nitrogen in semiconductor materials using the ^{14}N (p,α)^{11}C and ^{14}N(d,n)^{15}O nuclear reactions. Nucl. Instrum. Methods Phys. Res. B 50. https://doi.org/10.1016/0168-583X(90)90321-K.

Kraan, A.C., et al., 2015. Range verification methods in particle therapy: underlying physics and Monte Carlo modelling. Front. Oncol. 5 https://doi.org/10.3389/fonc.2015.00150.

Maxson, D.R., 1961. ^{16}O(p,α)^{13}N angular distributions at 13.5–18.1 MeV. Phys. Rev. 123 https://doi.org/10.1103/PhysRev.123.1304.

McCamis, R.H., Moss, G.A., Cameron, J.M., 1973. Total cross-section of ^{16}O(p,α)^{13}N from threshold to 7.7 MeV. Can. J. Phys. 51 https://doi.org/10.1139/p73-223.

Nero, A.V., Howard, A.J., 1973. ^{16}O(p,α)^{13N} cross-section measurements. Nucl. Phys. Sec. A 210. https://doi.org/10.1016/0375-9474(73)90503-4.

Nozaki, T., et al., 1966. The radioactivation analysis of semiconductor graphite for nitrogen by the ^{14}N(p, α) ^{11}C reaction. Bull. Chem. Soc. Jpn. 39 https://doi.org/10.1246/bcsj.39.2685.

Oelfke, U., Lam, G.K., Atkins, M.S., 1996. Proton dose monitoring with PET: quantitative studies in lucite. Phys. Med. Biol. 41 https://doi.org/10.1088/0031-9155/41/1/013.

Paganetti, H., et al., 2012. Range uncertainties in proton therapy and the role of Monte Carlo simulations. Phys. Med. Biol. 57 https://doi.org/10.1088/0031-9155/57/11/R99.

Parodi, K., et al., 2007. Clinical CT-based calculations of dose and positron emitter distributions in proton therapy using the Fluka Monte Carlo code. Phys. Med. Biol. 52 https://doi.org/10.1088/0031-9155/52/12/004.

Root data analysis framework v.5.34.30, 2015. https://root.cern.ch/.

Sajjad, M., Lambrecht, R.M., Wolf, A.P., 1986. Cyclotron isotopes and radiopharmaceuticals XXXVII. Excitation functions for the ^{16}O(p,α)^{13}N and ^{14}N(p,pn)^{13}N reactions. Radiochim. Acta 39. https://doi.org/10.1524/ract.1986.39.3.165.

Tárkányi, F.T., et al., 2019. Recommended nuclear data for medical radioisotope production: diagnostic positron emitters. J. Radioanal. Nucl. Chem. 319 https://doi.org/10.1007/s10967-018-6380-5.

Whitehead, A.B., Foster, J.S., 1958. Activation cross-sections for ^{12}C(p,pn)^{11}C,^{16}O (p,α)^{13}N and ^{19}F(p,pn)^{18}F. Can. J. Phys. 36 https://doi.org/10.1139/p58-132.

Ziegler, J., 1988. The Stopping and Range of Ions in Solids. https://doi.org/10.1016/b978-0-12-780621-1.50005-8.